Journal of Membrane Science 680 (2023) 121759

Contents lists available at ScienceDirect

Journal of Membrane Science

journal homepage: www.elsevier.com/locate/memsci

Engineering transport highways in microporous membranes for lithium extraction: The double role of covalent organic frameworks

Zhenshu Si [a], Zhe Zhang [b,*], Congcong Yin [a], Tong Ju [a], Mingjie Wei [a], Jun Huang [a], Yong Wang [a,**]

[a] State Key Laboratory of Materials-Oriented Chemical Engineering, and College of Chemical Engineering, Nanjing Tech University, Nanjing, 211816, Jiangsu, PR China
[b] School of Environmental Science and Engineering, Nanjing Tech University, Nanjing, 211816, Jiangsu, PR China

ARTICLE INFO

Keywords:
Covalent organic frameworks (COFs)
Transport highways
Microporous membranes
Lithium extraction
Ion separation

ABSTRACT

Microporous polyamide membranes that allow lithium ions to pass through easily but exclude magnesium ions hold vast potential in the lithium extraction from brine lakes. The efficacy, nevertheless, has long been limited by a trade-off that the magnesium/lithium selectivity is received at the expense of the permeability, arising from the highly cross-linked polyamide. This work describes that rationally lowering the internal density of polyamides by embedding functionalized covalent organic framework (COF) nanosheets can boost the selectivity and permeability simultaneously. A cationic COF, $TpTG_{Cl}$, is used to build transport highways in membranes, which shows the double role that not only lowers the polyamide density in a controllable way, but also strengthens the positive charge property. The resulting membrane exhibits a large water permeance of 19.6 L m^{-2} h^{-1} bar^{-1}, along with an excellent separation factor of up to 21.3 under a high magnesium/lithium ratio of 30. This engineering strategy offers a means by which charged and nanoporous two-dimensional frameworks can be leveraged as a booster for microporous membranes enabling fast and precise ion transports.

1. Introduction

With the rapid advancement of clean-energy industries represented by electric vehicles, smartphones and portable solar storages, demands for lithium have soared unprecedentedly, yet the scarcity of worldwide lithium resources looms large [1,2]. In addition to mineral ores, brine lakes reserve a large number of lithium ions (Li^+) that provide a reliable alternative for the acquisition of lithium resources [3]. The Li^+, however, frequently coexists with the high concentration of magnesium ions (Mg^{2+}) on the one hand, and the hydrated radius (3.8 Å) is in close proximity to Mg^{2+} (4.3 Å) on the other hand, posing a real-world challenge in lithium extraction [4]. To tackle the obstacles, significant effort has been devoted to extracting Li^+ from high Mg^{2+}/Li^+ ratio brines, including ion-sieves and the multistage solvent extraction [5]. These technologies have been shown to be feasible, but are subjected to the solution loss and the extensive use of toxic solvents.

Nanofiltration, a prevailing membrane separation technology that confers a more economically and environmentally sustainable way to separate Mg^{2+}/Li^+ ions [6,7]. The microporous polyamide is a much sought-after membrane material for the nanofiltration [8], which is fabricated by a fast and irreversible interfacial polymerization of polyfunctional amines and acyl chlorides [9–11]. The packing of linear chains along with networks cross-linking [12], collectively endow the polyamides with discretely distributed but interconnected free volumes at a subnanometer scale [13], which can be leveraged as the transport channel for membranes. Given that the nanofiltration is primarily determined by the mechanism of the size exclusion and Donnan effect [14,15], the microporous membranes carrying the positive charge can have a better rejection to Mg^{2+} [16,17]. Nevertheless, most polyamide membranes are negatively charged, arising from the residual acyl chlorides hydrolyzing into carboxyl groups [18,19]. Using positively charged polyelectrolytes, the polyethyleneimine (PEI) for example [20–22], as the monomer can circumvent the vulnerability, but inevitably yields polyamides with high cross-linking densities that do not have adequately interconnected channels, and consequently impede the transport of both Li^+ and water.

It has been revealed that the internal inhomogeneity of polyamide membranes governs the water-ions selectivity, and controlling the

* Corresponding author.
** Corresponding author.
E-mail addresses: zhangzhe@njtech.edu.cn (Z. Zhang), yongwang@njtech.edu.cn (Y. Wang).

https://doi.org/10.1016/j.memsci.2023.121759
Received 6 April 2023; Received in revised form 7 May 2023; Accepted 18 May 2023
Available online 19 May 2023

nanoscale density fluctuations would maximize separation performances [23]. This revelation enables envisioning that lowering, to a proper extent, the internal density of the polyelectrolyte-formed polyamide would significantly exclude Mg^{2+} rather than Li^{+}, while maintaining fast water permeation. In this context, the nano-heterogeneous membranes were prepared by a gradient modification from the membrane surface to its interior, using bidentate amines as the enabler. The membranes exhibited fast water permeation along with reasonable Mg^{2+}/Li^{+} selectivities [20,24–26]. Although those pioneering works have found exciting progresses, an overarching challenge remains thus far, for the boosting of Mg^{2+}/Li^{+} selectivities is usually achieved at the expense of the water permeance [27]. Covalent organic framework (COF) is a porous and crystalline framework material that possesses the ability to design at a molecular level and the structure-performance relationship is macroscopically predictable [28–31]. We thus envisioned that the COF featuring the innate positive charge, proper nanopores, and pure organic frameworks is capable of tuning the internal density of polyamides, which is amenable to realize fast and selective Li^{+} extraction.

In this contribution, the transport highways were engineered in microporous polyamide membranes using cationic COF nanosheets bearing sub-2-nm pores, showing the great promise in the lithium extraction from high Mg^{2+}/Li^{+} ratio brines. Amino-functionalized nanosheets were synthesized and embedded into microporous polyamides, which exhibited the double role that not only lowered the polyamide density in a controllable manner, but also boosted the positive charge property markedly. The microporous membrane displayed both ultrafast water permeation and remarkable selectivities, rendering advantages of higher sustainability over other existing extraction techniques.

2. Experimental section

2.1. Materials

1,3,5-Triformylphloroglucinol (Tp, 98%) and triaminoguanidinium chloride (TG_{Cl}, 95%) were provided by Jilin Chinese Academy of Sciences-Yanshen Technology Co., Ltd. Trimesoyl chloride (TMC, 99%) was brought from J&K Scientific. 4-(Dimethylamino) pyridine (DMAP, 99%) was obtained from Sigma-Aldrich. PEI (M_w: 600, 1800 and 70000 Da), polyethylene glycol (PEG, M_w: 200, 400, 600, 800, 1000 and 2000 Da), lithium chloride (LiCl, 99.0%), magnesium chloride hexahydrate ($MgCl_2$, 98.0%), 1,4-dioxane (99.0%), *N,N*-dimethylformamide (99.5%), and *n*-hexane (GC grade, 98.0%) were purchased from Aladdin. Acetone (98%), ethanol (99.7%) and potassium bromide (SP grade, 99.0%) were obtained from local supplier. Bovine serum albumin (BSA) and phosphate buffered saline (PBS) tablets were purchased from MP Biomedicals. Unless otherwise specified, all chemicals were used as received. Porous polyacrylonitrile (PAN) membranes were prepared through the process of nonsolvent induced phase separation according to a previous work [32], and the water permeance was ~900 L m^{-2} h^{-1} bar^{-1}. Deionized water was used in all experiments.

2.2. Synthesis of amino-functionalized $TpTG_{Cl}$ nanosheets

$TpTG_{Cl}$ nanosheets were synthesized using excess TG_{Cl} based on a previous report [33]. To an ampoule, Tp (0.2 mmol), TG_{Cl} (0.6 mmol, 3 equiv.) and a solvent mixture containing 2 mL of 1,4-dioxane and 0.6 mL of water were added sequentially. Afterward, the ampoule was subjected to sonication (300 W, 5 min) to afford a well dispersed mixture. The ampoule was degassed by three freeze-pump-thaw cycles, and was flame-sealed under vacuum. After solvothermal reaction at 120 °C for 72 h, the precipitate was isolated by filtration, and washed with *N, N*-dimethylformamide, water and acetone, respectively. Finally, as-collected precipitate was vacuum-dried at 60 °C for 12 h to afford powdery product. To prepare $TpTG_{Cl}$ nanosheet dispersion, 50 mg of $TpTG_{Cl}$ powder was dispersed in 500 mL of water, followed by sonication (300 W, 30 min). After that, the raw dispersion was centrifuged at 10000 rpm for 10 min, and the supernatant was collected as the final dispersion (concentration: ~0.01 mg mL^{-1}).

2.3. Membrane preparation

Membranes were prepared by interfacial polymerization. Typically, PAN substrates were soaked in an aqueous solution containing $TpTG_{Cl}$ nanosheets (0.01 mg mL^{-1}), PEI (70000 Da, 1.6%, w/v) and DMAP (0.02%, w/v) for 5 min. Then, the residual solution on the substrate surface was removed by a rubber roller, followed by contacting the substrate with an organic solution containing TMC dissolved in *n*-hexane (0.16%, w/v) for 1 min. After interfacial polymerization, as-prepared membranes were cured at 60 °C for 10 min, and were stored in water at room temperature for further use. This membrane was termed as COF-PA. Control membrane used for comparison was prepared by the same procedure in the absence of $TpTG_{Cl}$ nanosheets and DMAP, which was termed as PA.

2.4. Characterization

Fourier transform infrared spectra (FTIR) data of $TpTG_{Cl}$ and membranes were collected on a Nicolet 8700 spectrometer (Thermo Fisher Scientific) with the wavenumber ranging from 4000 to 800 cm^{-1}. Potassium bromide tablets were used for preparing powdery samples. Chemical compositions of $TpTG_{Cl}$ and membranes were further resolved by X-ray photoelectron spectroscopy (Shimadzu, Kratos, AXIS SUPRA). X-ray diffraction (XRD) diffractograms of $TpTG_{Cl}$ were characterized on a Smart Lab diffractometer (Rigaku) with the 2θ ranging from 2 to 40° and a step of 0.02°. Nitrogen adsorption isotherms of $TpTG_{Cl}$ powders were measured at 77 K on a BELSORP MAX analyzer (Microtrac). Surface area was obtained from the isotherm using the BET equation, and pore size distribution curves were calculated via the nonlocal density functional theory (NLDFT) model. Scanning electron microscopy (SEM) observation of $TpTG_{Cl}$ powders, membrane surfaces and cross sections was conducted on a S-4800 field-emission electron microscope (Hitachi). The operation voltage was 5 kV and the working current was 7 mA. All samples were sputtered with platinum coating to enhance the surface conductivity before imaging. High-resolution transmission electron microscopy (HRTEM) images were captured on a Tecnai F20 electron microscope (FEI) with an accelerating voltage of 200 kV. The microscope was configured with an energy-dispersive X-ray (EDX) detector. Samples were dispersed in ethanol, followed by drop-casting on a copper grid. The height profiles of $TpTG_{Cl}$ nanosheets and surface topographies of membrane were characterized by atomic force microscopy (AFM) on a XE-100 system (Park Systems) with tapping mode at a scan rate of 0.5 Hz. Zeta potential of membranes was analyzed by the streaming potential test on an electrokinetic analyzer (SurPASS, Anton Paar GmbH). The background electrolyte solution was KCl aqueous solution (0.1 mmol L^{-1}), and the test was conducted in the pH range of 4–9. The membrane hydrophilicity was measured by water contact angle on a Drop Meter A100P goniometer (MAIST).

2.5. Ion permeation test

Ion permeation test was conducted using a H-shaped cell with a membrane area of 0.79 cm^2. The membranes were mounted between two chambers of the cell by using O-rings to seal the membranes. 40 mL of 0.1 mol L^{-1} salt solutions ($MgCl_2$ or LiCl) were filled in the feed side, and 40 mL of water was filled in the filtrate side. The ion conductivity of the filtrate side was recorded by a S230–K electrical conductivity meter (Mettler-Toledo), and calibration curves were used to relate the conductivity to salt concentration. The pH of each side was controlled at ~6, and the two chambers were magnetically stirred to minimize concentration polarization near the membrane surface. The ion permeation rate

(J_i) can be calculated as follows:

$$J_i = (\Delta C\ V)\ /\ (A\ \Delta t) \quad (1)$$

where ΔC (mol L^{-1}) is the salt concentration of the filtrate. V (L) is volume of the filtrate. A (m^2) is the effective membrane area. Δt (h) is the testing duration.

2.6. Separation performance evaluation

A cross-flow filtration device equipped with three stainless-steel cells (active area, 7.1 cm^2) was used to evaluate the separation performance of membranes. The volume flow rate was 30 L h^{-1}, and the temperature was maintained at 20 °C using a heat exchanger. Prior to testing, all membranes were compacted at 6 bar for 30 min to reach a stable liquid permeation, and the performance tests were conducted at the same transmembrane pressure. The separation process was conducted at a pH value of ~6. The permeation flux (J_w, L m^{-2} h^{-1}) and permeance (P_w, L m^{-2} h^{-1} bar^{-1}) were calculated as following:

$$J_w = \Delta V\ /\ (A\ \Delta t) \quad (2)$$

$$P_w = J_w\ /\ \Delta p \quad (3)$$

where ΔV (L) is the volume of the filtrate permeating through the active membrane area A (m^2) with the designated duration Δt (h). Δp (bar) is the transmembrane pressure.

The rejection (R, %) of $MgCl_2$ and LiCl, as well as the rejection difference ratio (R_d) between $MgCl_2$ and LiCl were calculated as following:

$$R = \left(1 - C_p\ /\ C_f\right) \times 100\% \quad (4)$$

$$R_d = \left(1 - R_{LiCl}\ /\ R_{MgCl2}\right) \times 100\% \quad (5)$$

where C_p and C_f are the concentrations of the filtrate and the feed. R_{LiCl} and R_{MgCl2} are the rejections of LiCl and $MgCl_2$. The concentrations of the $MgCl_2$ and LiCl used as the feed were 1 g L^{-1}, and the concentration was determined by the electrical conductivity meter as described above.

For Mg^{2+}/Li^+ mixture, the concentration of LiCl was fixed at 0.5 g L^{-1}. The Mg^{2+}/Li^+ ratio was defined as the ratio of the mass concentration of $MgCl_2$ and LiCl in the feed, ranging from 1 to 30. For the two-stage nanofiltration test, a simulated salt-lake brine containing $MgCl_2$ and LiCl with a total concentration of 25.5 g L^{-1} and a Mg^{2+}/Li^+ ratio of 50 was prepared. The separation factor (SF) was calculated as follows:

$$SF = \left(C_{p,Li+}\ /\ C_{p,Mg2+}\right)\ /\ \left(C_{f,Li+}\ /\ C_{f,Mg2+}\right) \quad (6)$$

where $C_{p,Li+}$, $C_{p,Mg2+}$, $C_{f,Li+}$, $C_{f,Mg2+}$ are the concentrations of the Li^+ and Mg^{2+} in the filtrate and the feed, which were measured by inductively coupled plasma optical emission spectroscopy (ICP-OES, PerkinElmer, Avio 200).

A retention test using PEG with different molecular weights was performed to determine the molecular weight cut-off (MWCO), in which the MWCO can be defined as the molecular weight of PEG at the rejection of 90%. The concentration of the feed was 0.2 g L^{-1}, and the concentrations were determined by gel permeation chromatography (GPC, Waters 1515).

An anti-fouling test was conducted on the same cross-flow filtration device, using BSA as the protein foulant. The BSA aqueous solution was prepared with PBS tablets, and the concentration was 0.5 g L^{-1}. For the test, water and BSA solution were alternately filtrated across the COF-PA membrane for three cycles. The operating parameters during filtration were same as above.

3. Results and discussion

3.1. $TpTG_{Cl}$ nanosheet characterization

Fig. 1a depicts the synthetic route, in which Tp and TG_{Cl} proceeded a reversible Schiff-base condensation to yield the enol form first, and further converted into the chemically stable keto form after an irreversible tautomerism. For subsequent embedding, $TpTG_{Cl}$ is required to be amino-functionalized so that it can be covalently bonded into the polyamide via the amidation with TMC. Considering that the edge of the neat $TpTG_{Cl}$ possesses amino and aldehyde groups, TG_{Cl} was excessively added (in 3 equiv.) to ensure that the residual aldehyde can be further capped by amino groups, yielding the amino-functionalized $TpTG_{Cl}$. The formation of $TpTG_{Cl}$ was verified by the FTIR (Fig. 1b). The stretching bands (-C═O, 1639 cm^{-1} and H–C═O, 2897 cm^{-1}) of Tp, and the stretching band (N–H, 3318 cm^{-1}) of TG_{Cl} did not appear in the spectrum of $TpTG_{Cl}$. Furthermore, two stretching bands (C═C, 1587 cm^{-1} and C–N, 1309 cm^{-1}) emerged in $TpTG_{Cl}$ spectrum, indicating the existence of the β-ketoenamine linkage—the key feature of the keto form assigned to $TpTG_{Cl}$ [33]. XPS survey further validated the chemical structure of $TpTG_{Cl}$. In addition to the signals of C 1s, N 1s and O 1s, the Cl 2p signal was detected in $TpTG_{Cl}$ (Fig. 1c). Markedly, the organic nature endows $TpTG_{Cl}$ with a high carbon content (55.7%), and the existence of TG_{Cl} part accounts for the high ratio of nitrogen and oxygen elements (N/O ratio) which is of up to 2.20. In the high-resolution XPS spectrum (Fig. 1d), the N 1s signal can be mainly deconvoluted into three peaks [34,35], that is, the imine (398.1 eV), the amine (399.1 eV) and the C═N^+H (402.3 eV). By integration of the peak area of the amine, the content of which can be calculated as 44.4%, suggesting that the nitrogen existing in $TpTG_{Cl}$ was, to a large extent, in the form of an aliphatic amine, which in turn supports the occurrence of the amino functionalization. The crystalline structure of $TpTG_{Cl}$ was revealed by the XRD analysis (Fig. 1e), as two distinct peaks centering at 9.7 and 26.9° appeared in the diffractogram. They can be ascribed to the (100) and (001) planes, which is in good agreement with other work [33]. The N_2 adsorption-desorption analysis proved that $TpTG_{Cl}$ was microporous, for the fast uptake of N_2 occurred at the very low relative pressure (Fig. 1f). The surface area was calculated to be 135.7 m^2 g^{-1}, based on the BET equation (Fig. S1). By fitting the NLDFT model, the pore size distribution curve was obtained (Fig. 1g), and the pore size of $TpTG_{Cl}$ was centered at 1.3 nm, which is well in line with a previous report [33]. After a simple sonication treatment, $TpTG_{Cl}$ can be delaminated into nanosheets. SEM observation (Fig. 1h) confirmed the smooth and sheet-like morphology, with the lateral size ranging from a few to several dozens of microns. The thickness of $TpTG_{Cl}$ nanosheets was ~1.8 nm, according to the AFM measurement (Fig. 1i and j). HRTEM observation further verified the ultrathin nanosheets structure (Fig. 1k), and lattice fringes ascribed to the (001) plane with a lattice spacing of 0.33 nm can be clearly seen (Fig. 1l). Therefore, the HRTEM result was also supportive of the formation of crystalline structures, which is in accordance with the former XRD analysis. Moreover, EDX mapping (Fig. 1m) indicated the existence of all elements belonging to $TpTG_{Cl}$, and they were evenly distributed covering the entire nanosheets. Above results, collectively, validate that porous, crystalline and functionalized $TpTG_{Cl}$ nanosheets were successfully synthesized.

3.2. Membrane characterization

The COF-PA membrane was prepared by embedding $TpTG_{Cl}$ nanosheets in the polyamide matrix, while the PA membrane was prepared without embedding. XPS was used to dissect the chemical structures and compositions of membranes (Fig. 2a). In addition to the signals of C 1s, N 1s and O 1s assigned to both membranes, the Cl 2p signal was detected in COF-PA. According to the atomic concentration, the amount of carbon increased from 69.2% for PA to 73.0% for COF-PA, as a result of the $TpTG_{Cl}$ featuring pure organic backbones. Furthermore, the N/O ratio of

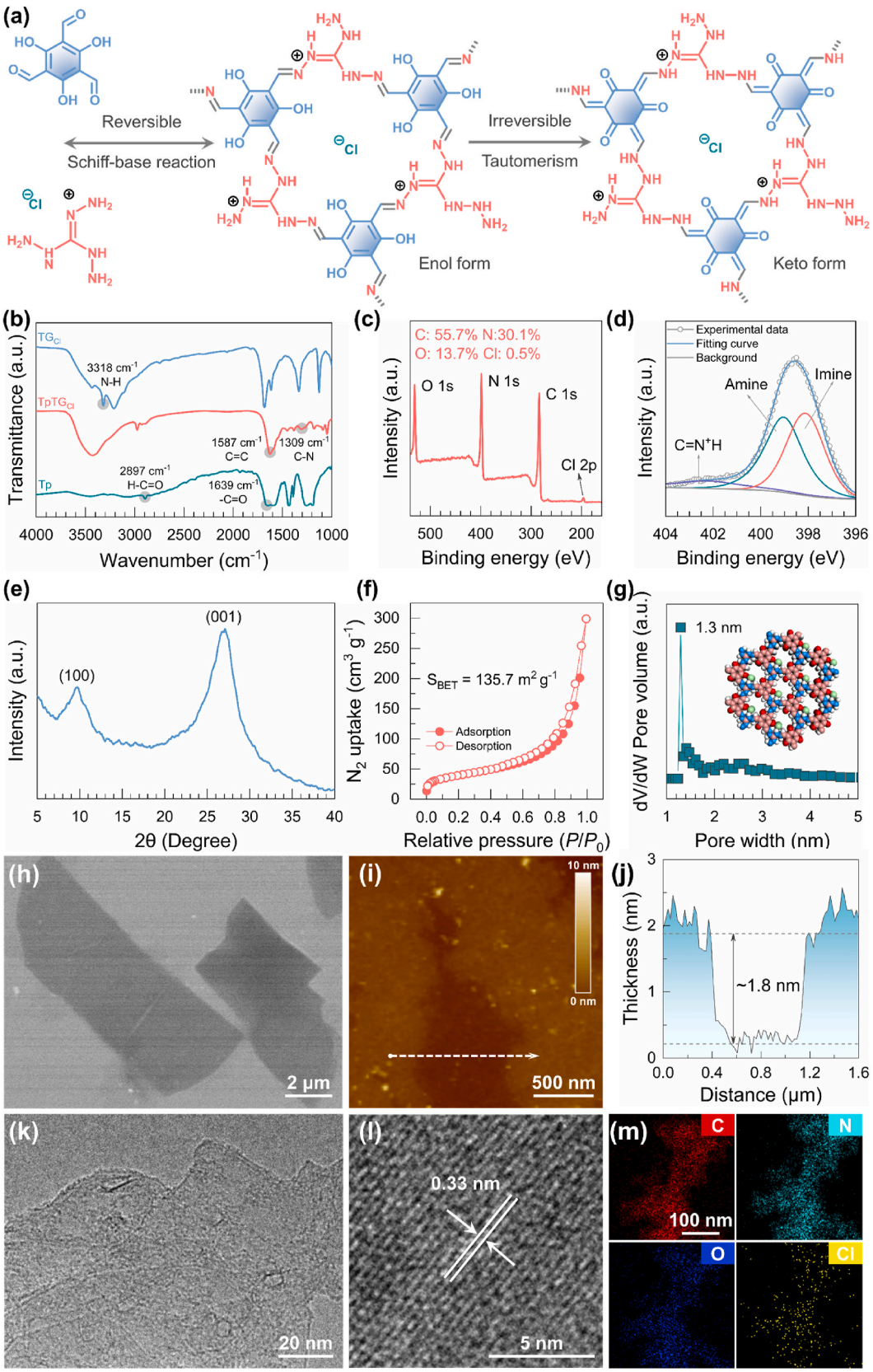

Fig. 1. Characterization of $TpTG_{Cl}$ nanosheets. (a) Synthetic route. (b) FTIR spectra. (c) Survey XPS spectrum. (d) High-resolution XPS spectrum of N 1s signal. (e) XRD diffractogram. (f) N_2 adsorption-desorption isotherm. (g) Pore size distribution curve (Inset shows section view of the crystal model). (h) SEM image. (i) AFM image (Inset shows height scale). (j) Height profile plot corresponding the white dash line in (i). (k) HRTEM image captured under low magnification. (l) HRTEM image captured under high magnification showing lattice fringes. (m) EDX mapping images for different elements.

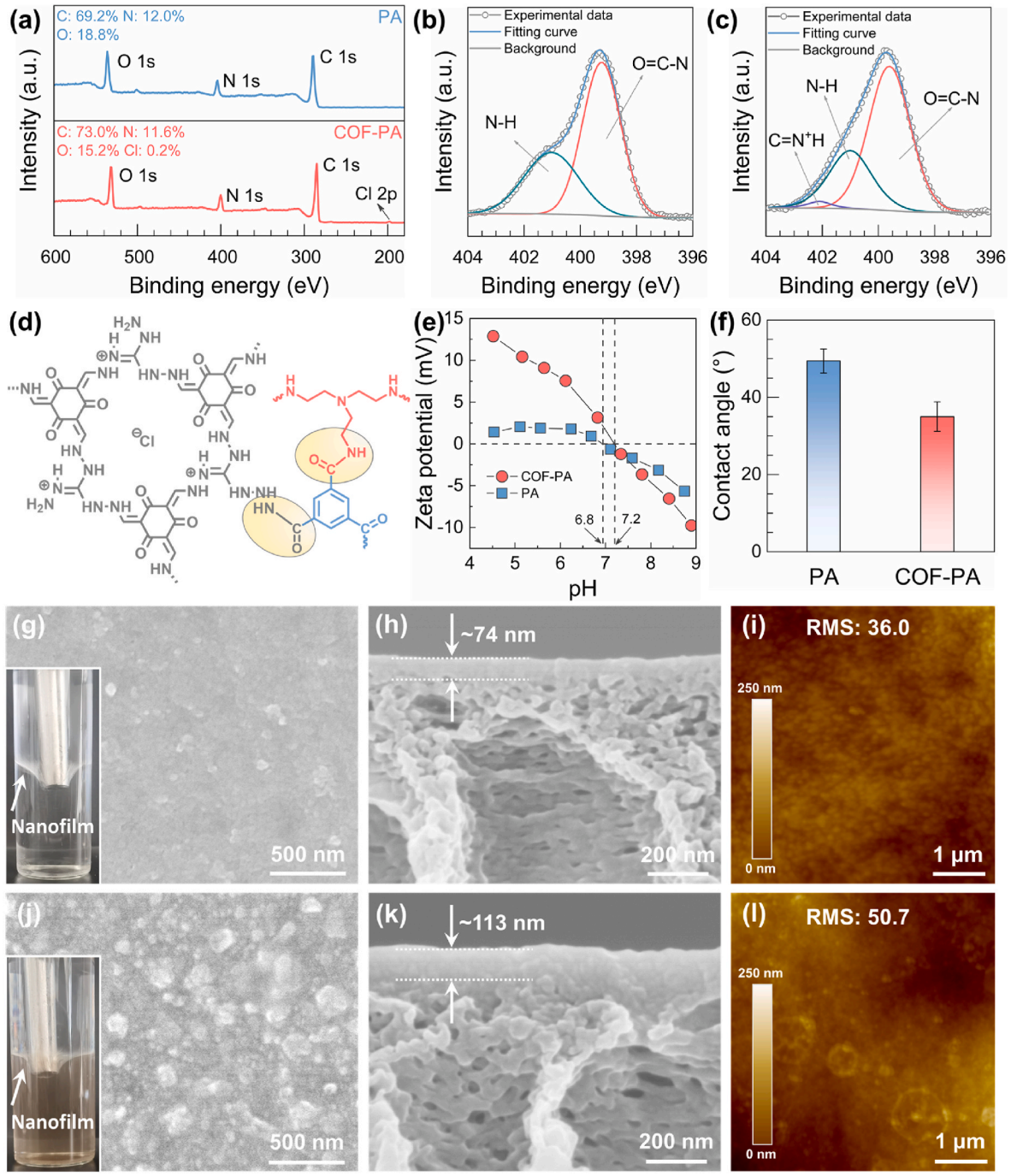

Fig. 2. Characterization of membranes. (a) Survey XPS spectra. (b) High-resolution XPS spectrum of N 1s signal of PA. (c) High-resolution XPS spectrum of N 1s signal of COF-PA. (d) Schematic structure of COF-PA. (e) Zeta potentials. (f) Water contact angles. Surface (g) and cross-sectional (h) SEM images of PA. Inset in (g) shows PA nanofilm formed at a free organic-aqueous interface. (i) AFM image of PA (Inset shows height scale). Surface (j) and cross-sectional (k) SEM images of COF-PA. Inset in (j) shows COF-PA nanofilm formed at a free organic-aqueous interface. (l) AFM image of COF-PA (Inset shows height scale).

COF-PA increased from 0.64 for PA to 0.76, on account of the high content of nitrogen of TG_{Cl} part in $TpTG_{Cl}$. It can be seen that, after the deconvolution, the N 1s signal of PA contains two peaks (O═C–N and N–H), ascribing to the amide groups of the polyamide (Fig. 2b) [36]. For COF-PA, apart from O═C–N and N–H, a new peak of C═N^+H emerged that can be assigned to $TpTG_{Cl}$ (Fig. 2c). Together, above results confirmed the chemical structure and composition of both membranes, and validated the successful embedding of $TpTG_{Cl}$ nanosheets in the polyamide matrix. With these dissections, the chemical structure of $TpTG_{Cl}$ nanosheets embedded polyamide matrices can be proposed (Fig. 2d). Based on our previous revelation, amino-functionalized COF nanosheets can be chemically linked by TMC with the catalysis of DMAP [32]. As shown in Fig. S2, $TpTG_{Cl}$ nanosheets were successfully converted into a nanofilm at a free organic-aqueous interface. Therefore, TMC was able to chemically link with both PEI and amino-functionalized $TpTG_{Cl}$ through the amidation, creating a matrix that comprised a polyamide network and $TpTG_{Cl}$ nanosheets. It should be noticed that the amidation exhibited a regioselective feature [37], as the amino groups exclusively existed on the edge of nanosheets. In other words, the chemical cross-linking occurred at the edge of the nanosheets, while the polyamide networks tended to aggregate on the plane of nanosheets [38]. In this vein, such aggregated polyamide, whose

networks did not chemically link with the nanosheets, would lower the local density of the polyamide matrix, generating a large number of free volumes between the nanosheets and the aggregated polyamide. Notably, the amidation between TMC and amino-functionalized $TpTG_{Cl}$ was required to be catalyzed by DMAP, as the steric hindrance potentially stemming from the cyclic structure of $TpTG_{Cl}$ would significantly reduce the reactivity. This phenomenon has been revealed in previous works [32,38], and was also agree with other works [39,40]. Zeta

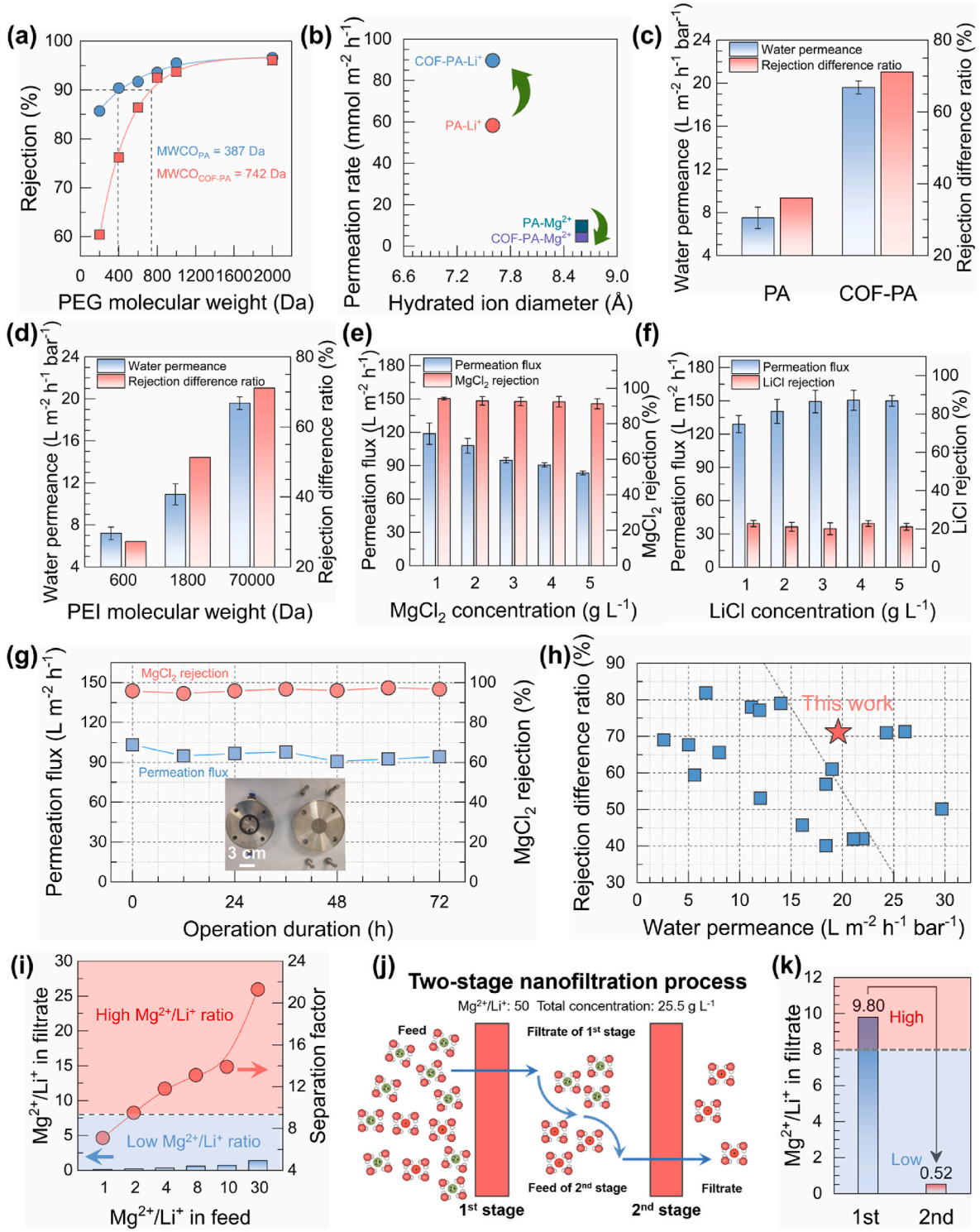

Fig. 3. Nanofiltration performances of membranes. (a) PEG retention curves of different membranes. (b) Permeation rates of Mg^{2+} and Li^+ plotted against the hydrated ion diameter. (c) Water permeance and rejection difference ratio of different membranes. (d) Effects of PEI molecular weight on water permeance and rejection difference ratio. (e) Effects of $MgCl_2$ concentration on permeation flux and rejection. (f) Effects of LiCl concentration on permeation flux and rejection. (g) Variation of permeation flux and $MgCl_2$ rejection during a duration of 72 h (Inset shows a disassembled stainless-steel cell used for the cross-flow test). (h) Summary of water permeance and rejection difference ratio of the state-of-the-art membranes reported in literatures (Details are listed in Table S4). (i) Effects of Mg^{2+}/Li^+ in feed on Mg^{2+}/Li^+ in filtrate and separation factor. (j) Schematic diagram showing a two-stage nanofiltration process. (k) Mg^{2+}/Li^+ in filtrate of the 1st and 2nd nanofiltration, respectively.

potentials further revealed the surface properties of membranes (Fig. 2e). Under acidic conditions, both membranes showed positively charged surfaces. Due to the branched PEI containing abundant aliphatic amines, the free amines that has not been consumed by TMC during the amidation would be protonated under such acidic environment, making the membrane surface positively charged [20]. Under acidic conditions, the COF-PA membrane exhibited a much stronger positive charge than that of PA, as a result of the guanidyl of $TpTG_{Cl}$ being positively charged [41]. Considering that the separation process was conducted at a pH value of ~6, the stronger positive charge would endow the membranes surface with the ability to repel high valence ions, which is beneficial to enhance the Donnan effect in the separation process of Mg^{2+}/Li^{+}. Moreover, after the embedding, the isoelectric point shifted from 6.8 for PA to 7.2 for COF-PA, due to the high protonation capability of guanidyl groups over a broad pH range [41]. In view of the high porosity and the guanidyl group of $TpTG_{Cl}$ nanosheets, the COF-PA membrane showed a better hydrophilicity than that of the PA membrane, which was demonstrated by the lower water contact angle of COF-PA (Fig. 2f).

The surface and cross-sectional morphologies of the PA and COF-PA membranes were observed via SEM and AFM imaging. The surface of PA displayed a typical morphology of nanofiltration membranes, in which the polyamide matrix was in relatively flat with small nodules (Fig. 2g). The thickness of the polyamide layer of PA was measured to be ~74 nm (Fig. 2h). AFM image also confirmed its relatively flat surface, of which the roughness (Root-mean-square, RMS) was measured to be 36.0 (Fig. 2i). Distinct from that of PA, the surface of COF-PA displayed an uneven morphology with large nodules (Fig. 2j). The discrepancy in morphology can be explained by a mediated interfacial polymerization as described in our previous works [42,43]. The diffusion rate of PEI would be slowed down to a certain extent by the charged and porous $TpTG_{Cl}$ nanosheets, resulting in a diffusion-driven instability, and thus creating a large number of nanoscale structures [44]. The thickness of the polyamide layer of COF-PA was ~113 nm, which was much thicker than that of PA (Fig. 2k). The $TpTG_{Cl}$ nanosheets adsorbed on the PAN substrate would be dragged into the reaction zone near the interface [45], as the interfacial polymerization continuously proceeded. Given the possible out-of-plane deformation as a result of the porous structure as well as the regioselectivity referred above, the nanosheets inside the matrix may do not show an ideally planar arrangement. Instead, a slanted arrangement with a somewhat out-of-plane deformation may probably occur [46], which in turn increased the thickness of the polyamide layer. This is also well in line with the rougher surface morphology having large nodules as shown in Fig. 2j. Furthermore, it is also likely that the lowered density and increased free volumes between the nanosheets and the aggregated polyamide as referred above, would contribute to the increased thickness. As shown in Fig. 2l, the RMS of the COF-PA membrane (50.7) was higher than that of the PA membrane, which indicated the rougher surface and was well in line with the observation from Fig. 2j. Overall, $TpTG_{Cl}$ nanosheets were chemically embedded into the polyamide matrix, enabling enhanced surface properties and distinctive morphologies.

3.3. Separation performance

To establish the structure-performance relationship, the separation performances of the COF-PA and PA membranes were evaluated. A PEG retention test was conducted to acquire the MWCO of membranes (Fig. 3a). It can be seen that, for the molecular weight of PEG being higher than 800 Da, both COF-PA and PA membranes showed similarly high rejections. Due to the electroneutrality of PEG molecules, the retention merely relies on the size exclusion rather than the Donnan effect. Thus, it is indicated that the membranes were defect-free, and the embedding of nanosheets did not compromise the rejection because of the good compatibility arising from the pure organic backbone as well as chemical cross-linking. By contrast, with the molecular weight of PEG decreasing from 800 to 200 Da, the COF-PA membrane exhibited much lower rejections than those of the PA membrane. This can be attributed to the sub-2-nm pores of $TpTG_{Cl}$ nanosheets, the lowered density and increased free volumes between the nanosheets and the aggregated polyamide as we have discussed above. Therefore, based on the retention curves, the MWCO of COF-PA and PA membranes was measured to be 742 and 387 Da, respectively.

To achieve an efficient separation process of Mg^{2+}/Li^{+}, the membrane should have the ability to exclude Mg^{2+}, but allow Li^{+} to pass through easily. Ion permeation tests that were driven by the concentration gradient using a H-shape cell were conducted (Fig. S3). Prior to testing, calibration curves were established to relate the conductivity to salt concentrations (Fig. S4). Thus, the ion conductivity and concentration of the filtrate side can be plotted as a function of time, respectively (Fig. S5). As shown in Fig. 3b, the permeation rates of the PA membrane for $Mg^{2+}$and Li^{+} were 9.5 and 58.3 mmol m^{-2} h^{-1}, respectively. After the embedding, the permeation rate of Mg^{2+} decreased to 4.9 mmol m^{-2} h^{-1}, while the permeation rate of Li^{+} increased to 89.7 mmol m^{-2} h^{-1}. The lowered density generated a large number of free volumes that allowed Li^{+} to pass through easily, and Mg^{2+} was subjected to a higher resistance than that of Li^{+} originating from the enhanced positive charge. It should be emphasized that the above test only measured the ion diffusion, which did not involve the convective flow that frequently occurred in the pressure-driven filtration process [47]. The latter influences, to a large extent, the transport of monovalent ions.

Thus, the nanofiltration performances of PA and COF-PA membranes were evaluated using a cross-flow model. For better comparison, the rejection difference ratio was used to quantitatively describe the rejection difference between $MgCl_2$ and LiCl (Fig. S6 showing the detail of rejections). It can be seen from Fig. 3c, the water permeance of PA was 7.5 L m^{-2} h^{-1} bar^{-1}, while the rejection difference ratio was 36.0. After the embedding, the water permeance of COF-PA increased to 19.6 L m^{-2} h^{-1} bar^{-1}, which is 2.6 times as high as that of the PA membrane. In addition, the rejection difference ratio reached 71.1, which is nearly twice as high as that of the PA membrane. For comparison, a PA membrane with the catalysis of DMAP, as well as a COF-PA membrane without the catalysis of DMAP were also prepared (Table S1). In the former case, the catalyst accelerated the reaction that has already been fast and irreversible, creating both a loosely structure polyamide and potentially enhanced negative charge originating from residual acyl chlorides by such fast reaction. Compared with the PA membrane, this membrane showed an improved water permeance but a compromised rejection to $MgCl_2$. In the latter case, the reaction of TMC and amino-functionalized $TpTG_{Cl}$ did not occur effectively, because of the presence of the steric hindrance of cyclic structure in $TpTG_{Cl}$. Thus, this membrane showed very similar performances with those of the PA membrane. In other words, the $TpTG_{Cl}$ nanosheets did not work without the catalysis of DMAP. In addition, the effects of $TpTG_{Cl}$ nanosheets concentrations on nanofiltration performances were also investigated (Table S2). It can be seen that, with the concentration decreasing, the membranes did not show high rejections to $MgCl_2$. This result indicates that the decreased $TpTG_{Cl}$ nanosheets concentrations would not provide adequate positive charge for a better rejection to Mg^{2+}. Overall, the $TpTG_{Cl}$ nanosheets played a double role that not only lowered the polyamide density in a controllable way, but also strengthened the positive charge property, enabling the fast and selective transport of both water and Li^{+}.

The PEI molecular weight on the nanofiltration performances was further investigated (Fig. S7 showing the detail of rejections). As shown in Fig. 3d, when PEI molecular weight was 600 Da, the membrane exhibited a very low water permeance of 7.2 L m^{-2} h^{-1} bar^{-1}, along with a low rejection difference ratio of 27.2. These performances were far worse than that of the COF-PA membrane, even worse than that of PA. With the molecular weight increasing to 1800 Da, the membrane showed a slightly boosted water permeance of 10.9 L m^{-2} h^{-1} bar^{-1}, and

the rejection difference ratio reached 51.3. In spite of the improved performances, they were not comparable with that of the COF-PA membrane. Above phenomena can be explained by the steric hindrance effect of branched PEI macromolecules [39]. For the PEI with a small molecular weight, the degree of branching is thought to be relatively low, thus allowing more amino groups to react with TMC. This would create a tight and highly cross-linked polyamide that could not generate sufficient free volumes used for water and the monovalent ion passing through. For the PEI with a large molecular weight, the highly branched structure would strengthen the steric hindrance effect that is beneficial to create a loosened polyamide. This is in favor of the fast permeation of both water and the monovalent ion. Therefore, above results well correlate the membrane structure and the nanofiltration performance.

Additionally, the nanofiltration performances using different concentration salts were also evaluated (Fig. 3e and f). With the salt concentration increasing, the rejection to $MgCl_2$ declined slightly, while the rejection to LiCl maintained almost unchanged. Due to the high protonation capability of guanidyl groups as indicated above, the $MgCl_2$ rejection did not decline significantly although the electrostatic shielding effect may be strengthened. During a long-term nanofiltration test, the permeation flux as well as the rejection of $MgCl_2$ both maintained almost unchanged over a period of 72 h (Fig. 3g). Moreover, benefitting from the relatively hydrophilic surface as discussed above, the COF-PA membrane exhibited a reasonable anti-fouling property (Fig. S8). The nanofiltration performance in terms of the water permeance and the rejection difference ratio was benchmarked against other state-of-the-art membranes reported in literatures. As shown in Fig. 3h, comparing with other membranes, the COF-PA membrane exhibited the both high water permeance and rejection difference ratio. These results, once again, highlighted the great potential of the COF-PA membrane in the extraction of Li^+ from Mg^{2+}.

Given the fact that Li^+ coexists most frequently with the high concentration of Mg^{2+}, which poses a demanding challenge for the Li^+ extraction. Thus, the effects of Mg^{2+}/Li^+ ratio on the nanofiltration performances were investigated (Fig. 3i and Table S3). With the Mg^{2+}/Li^+ ratio in the feed increasing from 1 to 30, the ratio in the filtrate always sustained at a nearly consistent level being lower than 2. Furthermore, the separation factor gradually increased as the Mg^{2+}/Li^+ ratio in the feed increasing, and the highest separation factor of 21.3 can be obtained under a high Mg^{2+}/Li^+ ratio of 30. Notably, a Mg^{2+}/Li^+ ratio of 8 is considered as a boundary to distinguish the high or low Mg^{2+}/Li^+ ratio, and the filtrate with a low Mg^{2+}/Li^+ ratio can be readily processed using the commercial solar evaporation-precipitation procedure [20]. Therefore, based on the above results, COF-PA membrane has the ability to process Mg^{2+}/Li^+ brine with a relatively broad range of salt concentrations. In addition, the COF-PA membrane was challenged to process highly concentrated Mg^{2+}/Li^+ brine using a two-stage nanofiltration process (Fig. 3j). A simulated salt-lake brine with a concentration of up to 25.5 g L^{-1} and a Mg^{2+}/Li^+ ratio of 50 was prepared. As shown in Fig. 3k, after the first nanofiltration, the Mg^{2+}/Li^+ ratio in the filtrate significantly reduced from 50 to 9.8. However, this value still falls in the range of a high ratio regime, which is unsatisfactory for the solar evaporation-precipitation procedure. Thus, the second nanofiltration was conducted using such filtrate as the feed, and the Mg^{2+}/Li^+ ratio can be successfully reduced to 0.52. Therefore, this membrane is capable of processing highly concentrated Mg^{2+}/Li^+ brine.

4. Conclusion

In summary, amino-functionalized $TpTG_{Cl}$ nanosheets were embedded into polyamide separation layers, endowing membranes with lowered internal densities and enhanced positive charges. $TpTG_{Cl}$ nanosheets were successfully synthesized, functionalized and thus embedded into the polyamide matrix. It was found that TMC can chemically link with both $TpTG_{Cl}$ nanosheets and the polyamide, and such embedding generated a large number of free volumes between the nanosheets and the aggregated polyamide by lowering the local density of the polyamide matrix. Moreover, the high protonation capability of guanidyl groups of $TpTG_{Cl}$ conferred the positively charged surface over a broad pH range. Due to the sub-2-nm pores of $TpTG_{Cl}$ nanosheets, the lowered density and increased free volumes, the resulting membrane showed a high water permeance of 19.6 L m^{-2} h^{-1} bar^{-1}, coupled with a remarkable separation factor of up to 21.3 under a Mg^{2+}/Li^+ ratio of 30. This work underlines that the charged and nanoporous COF is very promising for boosting the separation performance of extensively used polyamide nanofiltration membranes to meet the demand of fast and selective ion separations.

Author statement

Zhenshu Si: Investigation, Data curation, Writing-original draft. **Zhe Zhang:** Data curation, Writing-review & editing, Supervision. **Congcong Yin:** Investigation. **Tong Ju:** Investigation. **Mingjie Wei:** Results discussion, Funding acquisition. **Jun Huang:** Results discussion, Supervision. **Yong Wang**: Conceptualization, Writing-review & editing, Supervision, Funding acquisition. All authors have approved to the final version of the manuscript.

Declaration of competing interest

The authors declare no conflict of interest.

Data availability

Data will be made available on request.

Acknowledgments

Financial support from the National Natural Science Foundation of China (22278206, 21825803).

Appendix A. Supplementary data

Supplementary data to this article can be found online at https://doi.org/10.1016/j.memsci.2023.121759.

References

[1] G. Martin, L. Rentsch, M. Höck, M. Bertau, Lithium market research-global supply, future demand and price development, Energy Storage Mater. 6 (2017) 171–179.
[2] C. Liu, Y. Li, D. Lin, P.-C. Hsu, B. Liu, G. Yan, T. Wu, Y. Cui, S. Chu, Lithium extraction from seawater through pulsed electrochemical intercalation, Joule 4 (2020) 1459–1469.
[3] Y. Sun, Q. Wang, Y. Wang, R. Yun, X. Xiang, Recent advances in magnesium/lithium separation and lithium extraction technologies from salt lake brine, Sep. Purif. Technol. 256 (2021), 117807.
[4] A. Battistel, M.S. Palagonia, D. Brogioli, F. La Mantia, R. Trócoli, Electrochemical methods for lithium recovery: a comprehensive and critical review, Adv. Mater. 32 (2020), 1905440.
[5] G. Liu, Z. Zhao, A. Ghahreman, Novel approaches for lithium extraction from salt-lake brines: a review, Hydrometallurgy 187 (2019) 81–100.
[6] X. Li, Y. Mo, W. Qing, S. Shao, C.Y. Tang, J. Li, Membrane-based technologies for lithium recovery from water lithium resources: a review, J. Membr. Sci. 591 (2019), 117317.
[7] J. Hou, H. Zhang, A.W. Thornton, A.J. Hill, H. Wang, K. Konstas, Lithium extraction by emerging metal-organic framework-based membranes, Adv. Funct. Mater. 31 (2021), 2105991.
[8] J.R. Werber, C.O. Osuji, M. Elimelech, Materials for next-generation desalination and water purification membranes, Nat. Rev. Mater. 1 (2016), 16018.
[9] E.L. Wittbecker, P.W. Morgan, Interfacial polycondensation. I, J. Polym. Sci., Part A: Polym. Chem. 34 (1996) 521–529.
[10] P.W. Morgan, S.L. Kwolek, Interfacial polycondensation. II. fundamentals of polymer formation at liquid interfaces, J. Polym. Sci., Part A: Polym. Chem. 34 (1996) 531–559.
[11] F. Zhang, J. Fan, S. Wang, Interfacial polymerization: from chemistry to functional materials, Angew. Chem. Int. Ed. 59 (2020) 21840–21856.

[12] Z. Jiang, R. Dong, A.M. Evans, N. Biere, M.A. Ebrahim, S. Li, D. Anselmetti, W. R. Dichtel, A.G. Livingston, Aligned macrocycle pores in ultrathin films for accurate molecular sieving, Nature 609 (2022) 58–64.
[13] X. Zhou, Z. Wang, R. Epsztein, C. Zhan, W. Li, J.D. Fortner, T.A. Pham, J.-H. Kim, M. Elimelech, Intrapore energy barriers govern ion transport and selectivity of desalination membranes, Sci. Adv. 6(48) eabd9045.
[14] C. Boo, Y. Wang, I. Zucker, Y. Choo, C.O. Osuji, M. Elimelech, High performance nanofiltration membrane for effective removal of perfluoroalkyl substances at high water recovery, Environ. Sci. Technol. 52 (2018) 7279–7288.
[15] R. Epsztein, R.M. DuChanois, C.L. Ritt, A. Noy, M. Elimelech, Towards single-species selectivity of membranes with subnanometre pores, Nat. Nanotechnol. 15 (2020) 426–436.
[16] A. Razmjou, M. Asadnia, E. Hosseini, A. Habibnejad Korayem, V. Chen, Design principles of ion selective nanostructured membranes for the extraction of lithium ions, Nat. Commun. 10 (2019) 5793.
[17] F. Xu, L. Dai, Y. Wu, Z. Xu, Li^+/Mg^{2+} separation by membrane separation: the role of the compensatory effect, J. Membr. Sci. 636 (2021), 119542.
[18] X. Lu, M. Elimelech, Fabrication of desalination membranes by interfacial polymerization: history, current efforts, and future directions, Chem. Soc. Rev. 50 (2021) 6290–6307.
[19] M.-B. Wu, H. Ye, Z.-Y. Zhu, G.-T. Chen, L.-L. Ma, S.-C. Liu, L. Liu, J. Yao, Z.-K. Xu, Positively-charged nanofiltration membranes constructed via gas/liquid interfacial polymerization for Mg^{2+}/Li^+ separation, J. Membr. Sci. 644 (2022), 119942.
[20] H. Peng, Q. Zhao, A nano-heterogeneous membrane for efficient separation of lithium from high magnesium/lithium ratio brine, Adv. Funct. Mater. 31 (2021), 2009430.
[21] H. Li, Y. Wang, T. Li, X.-K. Ren, J. Wang, Z. Wang, S. Zhao, Nanofiltration membrane with crown ether as exclusive Li^+ transport channels achieving efficient extraction of lithium from salt lake brine, Chem. Eng. J. 438 (2022), 135658.
[22] F. Soyekwo, H. Wen, D. Liao, C. Liu, Nanofiltration membranes modified with a clustered multiquaternary ammonium-based ionic liquid for improved magnesium/lithium separation, ACS Appl. Mater. Interfaces 14 (2022) 32420–32432.
[23] T.E. Culp, B. Khara, K.P. Brickey, M. Geitner, T.J. Zimudzi, J.D. Wilbur, S.D. Jons, A. Roy, M. Paul, B. Ganapathysubramanian, A.L. Zydney, M. Kumar, E.D. Gomez, Nanoscale control of internal inhomogeneity enhances water transport in desalination membranes, Science 371 (2021) 72–75.
[24] Y. Feng, H. Peng, Q. Zhao, Fabrication of high performance Mg^{2+}/Li^+ nanofiltration membranes by surface grafting of quaternized bipyridine, Sep. Purif. Technol. 280 (2022), 119848.
[25] X. Liu, Y. Feng, Y. Ni, H. Peng, S. Li, Q. Zhao, High-permeance Mg^{2+}/Li^+ separation nanofiltration membranes intensified by quadruple imidazolium salts, J. Membr. Sci. 667 (2023), 121178.
[26] H. Peng, Y. Hu, S. Li, J. Rao, Q. Zhao, Sulfonium-polyamide membranes for high flux Mg^{2+}/Li^+ separation, J. Membr. Sci. 674 (2023), 121515.
[27] H.B. Park, J. Kamcev, L.M. Robeson, M. Elimelech, B.D. Freeman, Maximizing the right stuff: the trade-off between membrane permeability and selectivity, Science 356 (2017) eaab0530.
[28] R. Liu, K.T. Tan, Y. Gong, Y. Chen, Z. Li, S. Xie, T. He, Z. Lu, H. Yang, D. Jiang, Covalent organic frameworks: an ideal platform for designing ordered materials and advanced applications, Chem. Soc. Rev. 50 (2021) 120–242.
[29] L. Deng, Z. Ding, X. Ye, D. Jiang, Covalent organic frameworks: chemistry of pore interface and wall surface perturbation and impact on functions, Acc. Mater. Res. 3 (2022) 879–893.
[30] Z. Li, T. He, Y. Gong, D. Jiang, Covalent organic frameworks: pore design and interface engineering, Acc. Mater. Res. 53 (2020) 1672–1685.
[31] H. Wang, M. Wang, X. Liang, J. Yuan, H. Yang, S. Wang, Y. Ren, H. Wu, F. Pan, Z. Jiang, Organic molecular sieve membranes for chemical separations, Chem. Soc. Rev. 50 (2021) 5468–5516.
[32] Z. Zhang, C. Yin, G. Yang, A. Xiao, X. Shi, W. Xing, Y. Wang, Stitching nanosheets of covalent organic frameworks to build aligned nanopores in nanofiltration membranes for precise ion separations, J. Membr. Sci. 618 (2021), 118754.
[33] S. Mitra, S. Kandambeth, B.P. Biswal, M.A. Khayum, C.K. Choudhury, M. Mehta, G. Kaur, S. Banerjee, A. Prabhune, S. Verma, S. Roy, U.K. Kharul, R. Banerjee, Self-exfoliated guanidinium-based ionic covalent organic nanosheets (iCONs), J. Am. Chem. Soc. 138 (2016) 2823–2828.
[34] W. Ji, L. Xiao, Y. Ling, C. Ching, M. Matsumoto, R.P. Bisbey, D.E. Helbling, W. R. Dichtel, Removal of GenX and perfluorinated alkyl substances from water by amine-functionalized covalent organic frameworks, J. Am. Chem. Soc. 140 (2018) 12677–12681.
[35] Z. Guo, H. Wu, Y. Chen, S. Zhu, H. Jiang, S. Song, Y. Ren, Y. Wang, X. Liang, G. He, Y. Li, Z. Jiang, Missing-linker defects in covalent organic framework membranes for efficient CO_2 separation, Angew. Chem. Int. Ed. 61 (2022), e202210466.
[36] Z. Wang, Z. Wang, S. Lin, H. Jin, S. Gao, Y. Zhu, J. Jin, Nanoparticle-templated nanofiltration membranes for ultrahigh performance desalination, Nat. Commun. 9 (2018) 2004.
[37] T. Huang, T. Puspasari, S.P. Nunes, K.-V. Peinemann, Ultrathin 2D-layered cyclodextrin membranes for high-performance organic solvent nanofiltration, Adv. Funct. Mater. 30 (2020), 1906797.
[38] Z. Zhang, C. Yin, X. Shi, G. Yang, Y. Wang, Masking covalent organic frameworks (COFs) with loose polyamide networks for precise nanofiltration, Sep. Purif. Technol. 283 (2022), 120233.
[39] J. Qin, S. Lin, S. Song, L. Zhang, H. Chen, 4-Dimethylaminopyridine promoted interfacial polymerization between hyperbranched polyesteramide and trimesoyl chloride for preparing ultralow-pressure reverse osmosis composite membrane, ACS Appl. Mater. Interfaces 5 (2013) 6649–6656.
[40] H. Peng, W.-H. Zhang, W.-S. Hung, N. Wang, J. Sun, K.-R. Lee, Q.-F. An, C.-M. Liu, Q. Zhao, Phosphonium modification leads to ultrapermeable antibacterial polyamide composite membranes with unreduced thickness, Adv. Mater. 32 (2020), 2001383.
[41] S. Zhang, R. Zhang, R. Li, Z. Zhang, Y. Li, H. Deng, J. Zhao, T. Gu, M. Long, X. Wang, S. Zhang, Z. Jiang, Guanidyl-incorporated nanofiltration membranes toward superior Li^+/Mg^{2+} selectivity under weakly alkaline environment, J. Membr. Sci. 663 (2022), 121063.
[42] Z. Zhang, X. Shi, R. Wang, A. Xiao, Y. Wang, Ultra-permeable polyamide membranes harvested by covalent organic framework nanofiber scaffolds: a two-in-one strategy, Chem. Sci. 10 (2019) 9077–9083.
[43] D. Ma, Z. Zhang, S. Xiong, J. Zhou, Y. Wang, Additive manufacturing of defect-healing polyamide membranes for fast and robust desalination, J. Membr. Sci. 671 (2023), 121407.
[44] Z. Tan, S. Chen, X. Peng, L. Zhang, C. Gao, Polyamide membranes with nanoscale turing structures for water purification, Science 360 (2018) 518–521.
[45] N.A. Khan, J. Yuan, H. Wu, T. Huang, X. You, A.U. Rahman, C.S. Azad, M.A. Olson, Z. Jiang, Covalent organic framework nanosheets as reactive fillers to fabricate free-standing polyamide membranes for efficient desalination, ACS Appl. Mater. Interfaces 12 (2020) 27777–27785.
[46] H. Li, J.-L. Brédas, Large out-of-plane deformations of two-dimensional covalent organic framework (COF) sheets, J. Phys. Chem. Lett. 9 (2018) 4215–4220.
[47] S. Gao, Y. Zhu, Y. Gong, Z. Wang, W. Fang, J. Jin, Ultrathin polyamide nanofiltration membrane fabricated on brush-painted single-walled carbon nanotube network support for ion sieving, ACS Nano 13 (2019) 5278–5290.